ACS APPLIED MATERIALS & INTERFACES

Research Article

www.acsami.org

Structural Study of Octacalcium Phosphate Bone Cement Conversion in Vitro

Marco Fosca,[†,‡] Vladimir S. Komlev,[§] Alexander Yu. Fedotov,[§] Ruggero Caminiti,[‡] and Julietta V. Rau*[,†]

[†]Istituto di Struttura della Materia, Consiglio Nazionale delle Ricerche, Via del Fosso del Cavaliere, 100-00133 Rome, Italy

[‡]Dipartimento di Chimica, Università di Roma "La Sapienza", Piazzale Aldo Moro, 5-00185 Rome, Italy

[§]A.A. Baikov Institute of Metallurgy and Materials Science, Russian Academy of Sciences, Leninsky prospect 49, 119991 Moscow, Russia

ABSTRACT: The nature of precursor phase during the biomineralization process of bone tissue formation is still controversial. Several phases were hypothesized, among them octacalcium phosphate. In this study, an in situ monitoring of structural changes, taking place upon the octacalcium phosphate bone cement hardening, was carried out in the presence of biopolymer chitosan and simulated body fluid (SBF). Several systems with different combinations of components were studied. The energy dispersive X-ray diffraction was applied to study the structural changes in real time, while morphological properties of the systems were investigated by the scanning electron microscopy. The obtained results evidence that final hydroxyapatite phase is formed only in the presence of chitosan and/or SBF, providing new insights into the in vivo biomineralization mechanism and, consequently, favoring the development of new approaches in biomaterials technology.

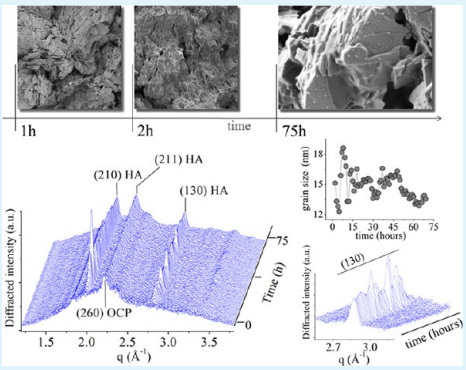

KEYWORDS: *octacalcium phosphate, bone cement, chitosan, simulated body fluid, hardening mechanism, energy dispersive X-ray diffraction*

1. INTRODUCTION

A cement system, in general, is a heterogeneous composition system that includes one or more solid dispersed active phases (powder/s) and a hardening liquid (binder). After mixing, the interaction of these components takes place followed by the processes of cement's setting and hardening. Two types of interactions can be distinguished: acid−base reaction with the formation of a neutral compound and the reaction of hydrolysis of the metastable phosphate in an aqueous medium. Calcium phosphate cements are used for nonload-bearing bone fractures and small defects and appear to be very promising materials for bone grafting applications.[1] Moreover, these cements can be easily manipulated and possess good biocompatibility.

The mineral part of the natural bone tissue is mainly composed of biological apatite, which is nonstoichiometric and contains various substitutions. Recently, it was ascertained that octacalcium phosphate (OCP) is a possible intermediate phase during the hydroxyapatite (HA) crystallization from aqueous solution under certain conditions[2] and that HA crystals inherit the morphology of the plate-shaped OCP crystals.[3] A similar situation might take place during the biomineralization process in vivo. It has been reported[4,5] that OCP induces the new bone tissue formation, compared to nonosteoinductive HA. It is possible that OCP has increased adsorption ability of some important morphogenetic proteins involved in osteosynthesis or contributes to the increase of the local concentration of calcium ions, taking part in the apatite precipitation.[5] Moreover, OCP is resorbable, favoring the kinetics of biodegradation and new bone formation.[6] Since OCP is the probable precursor of HA crystallization in vivo, the present study is important for the development of the new OCP-based bone cements and for the understanding of the mechanism of the OCP transformation under the conditions, simulating those in vivo (presence of biopolymer and simulating body fluid environment).

The reason why chitosan was used in the present research instead of collagen is that the latter, being one of the organic components of human bone and showing excellent biological properties, has several disadvantages. They include the fact that it is difficult to obtain it from a patient, and nowadays, most collagen materials are of animal origin. Moreover, collagen is characterized by an uncontrolled degradation rate, and it could also lead to immunological reactions and inflammation. To overcome these disadvantages, in the past decade, a significant attention in the field of bone tissue engineering has been given to chitosan-based biomaterials, due to their biodegradability, biocompatibility, and resemblance with the natural extracellular matrix. Furthermore, the addition of chitosan to bone cement aims to modulate its properties, such as hardening behavior.[7,8]

The scope of the present study is the real-time monitoring of structural transformations and kinetics of several OCP-based cement formulations under physiological conditions. The formation of new phases was in situ monitored by the energy

Received: August 28, 2012
Accepted: October 22, 2012
Published: October 22, 2012

   dx.doi.org/10.1021/am301809y | *ACS Appl. Mater. Interfaces* 2012, 4, 6202−6210

dispersive X-ray diffraction technique (EDXRD), allowing one to obtain a 3D map of diffraction patterns, collected as a function of the scattering parameter and of time.[9,10] The EDXRD structural investigations were complemented with the scanning electron microscopy (SEM) morphological studies.

2. EXPERIMENTAL SECTION

2.1. Synthesis of Octacalcium Phosphate Powder. OCP powder was obtained according to the wet precipitation synthesis method:[11]

$$8Ca(CH_3COO)_2 + 6Na_2HPO_4 + 5H_2O \rightarrow Ca_8H_2(PO_4)_6 \times 5H_2O + 12CH_3COONa + 4CH_3COOH \quad (1)$$

Chemically pure calcium acetate monohydrate (Sigma-Aldrich, ≥99.0%) and disodium hydrophosphate (Merck, 99.5%) were used to obtain OCP. Calcium acetate monohydrate solution (0.04 mol/L, 250 mL) and disodium hydrophosphate solution (0.03 mol/L, 250 mL) were heated at 90 °C and pH = 5.5. The disodium hydrophosphate solution was added dropwise to the calcium acetate solution and stirred during the precipitation. After 1 h, the precipitates were filtered and dried at room temperature. Phase composition of the obtained substances was confirmed by the conventional XRD analysis (diffractometer Shimadzu XRD-6000, Cu Kα_1 radiation, card number 26-1056).[12]

2.2. Hardening Liquid Preparation. A sodium silicate solution ($Na_2O-SiO_2-H_2O$ system) with pH = 9.5, water content of about 50−60%, and with an as-batched silicate modulus of about 3 was prepared and used as the hardening liquid (HL).[13] For its preparation, a commercial glass (PQ Corporation) with a nominal composition of about 20 mol % Na_2O and 80 mol % SiO_2 was used.

2.3. Simulated Body Fluid Preparation. To investigate in vitro behavior, a simulated body fluid (SBF) solution with ion concentrations (Na^+ 142.0, K^+ 5.0, Ca^{2+} 2.5, Mg^{2+} 1.5, Cl^- 147.8, HCO_3^- 4.2, HPO_4^{2-} 1.0, SO_4^{2-} 0.5, all in mM) nearly equal to those of the human blood plasma at 36.5 °C was prepared according to ref 14. The SBF was obtained by dissolving reagent-grade chemicals of NaCl (Panreac, 99.5%), $NaHCO_3$ (Sigma-Aldrich, 99.5%), KCl (Panreac, 99.5%), $K_2PO_4 \times 3H_2O$ (Fluka, ≥99.0%), $MgCl_2 \times 6H_2O$ (Sigma-Aldrich, ≥99.0%), $CaCl_2$ (Sigma, ≥96.0%), and Na_2SO_4 (Sigma-Aldrich, ≥99.0%) into distilled water and buffered at pH = 7.4 with tris-hydroxymethyl-aminomethane ($(HOCH_2)_3CNH_2$) (Tris) (Merck, 99.8%) and 1 M hydrochloric acid (Sigma, 36.5−38.0%, BioReagent) at 36.5 °C.

2.4. Cement Pastes Preparation. OCP powder was added to the hardening liquid and intimately mixed on a flat laboratory glass, until a dense homogeneous creamy paste was formed (about 1 min). The liquid-to-powder ratio was about 1:1 (by mass). In the systems containing chitosan, this latter was first mixed with the OCP powder in the proportion of 1:0.2 mass % (OCP/chitosan) and subsequently mixed with the hardening liquid in the proportion of 1:1 (by mass). Water-soluble, low molecular weight (38.2 kDA) chitosan (Aldrich) was used. In the case of cement paste soaked in SBF, the simulating body fluid was added to the paste 15 min after its preparation. The average mass sample of SBF was about 5× the mass of the cement sample to be soaked. This proportion was the same every single time.

2.5. Setting Time Measurements. The setting times of the prepared cement pastes were evaluated using the tip (1 mm diameter) of a Vicat needle with a 400 g load (according to ISO standard 1566) to make a perceptible circular indentation on the surface of the cement samples.

2.6. pH Measurements. The pH measurements were performed as follows: samples (1 g) of crushed cements were placed into a 100 mL volume flask, and distilled water was added up to the 50 mL volume. The pH value was measured after 1 h of soaking time at room temperature using a Hanna Instruments HI 8314 pH meter (HANNA, Germany).

2.7. Energy Dispersive X-ray Diffraction Measurements. The Energy dispersive X-ray diffraction method was applied to follow the structural modifications, taking place upon cement hardening, by collecting sequences of diffraction patterns in real time. The acquisition time of each pattern was set at 60 s, and the overall observation time was up to 160 h. The EDXRD measurements were performed by a noncommercial apparatus.[15] The energy spectrum of the primary beam is produced by a W-anode X-ray tube (supplied at 55 keV) and, after it is modulated by the interaction with the sample, the resulting diffracted radiation is analyzed by an ultra pure Ge single crystal solid-state detector. In this way, the reciprocal space scan necessary to reconstruct the diffraction pattern, i.e., the scan of the scattering parameter $q = a\ E \sin\theta$ (where q is the normalized momentum transfer magnitude, a is a constant, E is the energy of the incident X-ray beam, and 2θ is the scattering angle), is carried out electronically. Although, in the energy dispersive (ED) mode, the q-resolution is lower; its main advantage over the conventional angular dispersive counterpart (ADXRD) in performing X-ray diffraction experiments is that the geometric setup is kept fixed during the acquisition of the patterns, which simplifies the experimental geometry and prevents systematic angular errors, as well as possible misalignments. This feature, combined with a much faster data acquisition (the number of photons contained in the white component of the primary beam spectrum is about 2 orders of magnitude higher than the number of photons concentrated in the fluorescence lines), makes this technique particularly suitable for the in situ time-resolved measurements, allowing one to follow the real-time structural changes occurring on time scales varying from a few minutes up to several weeks.

In the case of EDXRD, the data analysis is more complicated than that of ADXRD.[15] Particular care must be taken for the method for estimating the grain size from the energy dispersive diffraction patterns, because the Scherrer formula, which is applied to the angular dispersive case only, must be suitably modified. The procedure, based on the Laue equations, is fully described elsewhere.[7,9]

Several diffraction patterns were collected as preliminary tests on the pristine cement powder and final cements at various scattering angles, in order to make a wide q-scan for individuating the q-region of interest and making an accurate assignment of the diffraction peaks. Since, according to the value of the high voltage supply reported above, the maximum beam energy corresponds to 55 keV, progressively increasing the scattering angle 2θ, the sequence of Bragg peaks could be easily individuated. All the EDXRD measurements, presented in this work, were collected in transmission geometry, keeping the experimental conditions unchanged during the acquisitions, that is $2\theta = 8°$ and $E_{max} = 55$ kV. The q-range so-explored was from 1.0 up to 4.0 Å^{-1}. The optical path was defined by three square collimation slits, their aperture being (300 × 300) μm. After preparation, cement pastes were immediately placed in the sample holder of the optical center of the diffractometer, and the EDXRD patterns were collected.

2.8. X-Ray Diffraction. In a few cases, phase composition of the obtained substances was analyzed by the conventional ADXRD technique (Shimadzu XRD-6000 (Japan), Ni-filtered Cu Kα_1 target, λ = 1.54183 Å). Samples were scanned from $2\theta = 3°$ to 41° with a step size of 0.02° and a preset time of 5 s.

2.9. Scanning Electron Microscopy Characterization. SEM apparatus (TESCAN VEGA II (Czech Republic) and Carl Zeiss NVision 40 (Germany)), working in secondary and backscattered electron modes, were used for morphological studies of the cement samples. In the case of the TESCAN VEGA II apparatus, the samples were sputter-coated, prior to imaging, with a 25 nm-thick gold layer to impart electrical conductivity to the specimen surface; whereas the Carl Zeiss NVision 40 instrument provides the possibility of investigating nonconductive samples using a local charge compensation method. Both of the SEM apparatus are coupled with a system for EDXS (energy-dispersive X-ray spectroscopy) microanalysis, allowing one to execute qualitative/quantitative analysis of the elements. SEM images were registered at various time intervals after cement samples

preparation, such as 1, 2, 70, 75, 110, and 125 h. SEM micrographs were taken at various magnifications (from 5000 up to 75 000).

3. RESULTS

3.1. OCP Powder Soaked in SBF. In this case, the OCP powder was first mixed with a small amount of the SBF solution to prepare a paste (in the proportion of 1:1 by mass, 0.5 g of OCP/5.5 mL of SBF). Afterward, the paste was soaked in SBF. The so-obtained system was placed in the sample holder of the optical center of the EDXRD apparatus. The spectra were collected for a total duration of 160 h. The diffraction patterns were registered every 10 min for the first hour and every 15 min for the remaining 159 h. In Figure 1, the sequences of 3D

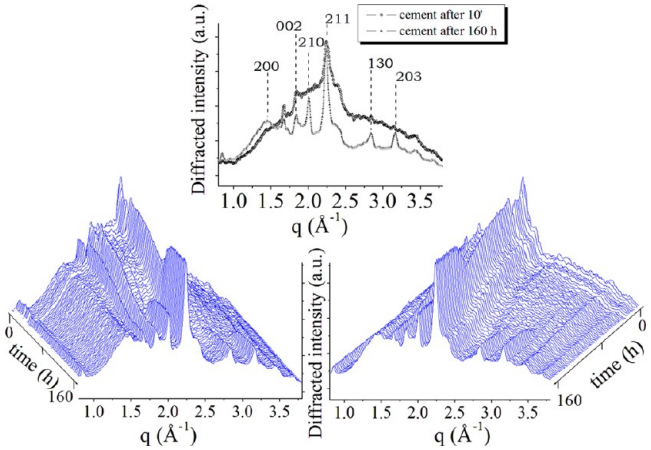

Figure 1. Sequence of EDXRD patterns collected upon the OCP powder soaked in SBF. Lower part shows low-q perspective (left) and high-q perspective (right) of the same sequence of patterns. In the top center, a comparison between spectra, collected at the beginning (10 min) and at the end (160 h) of the process, is shown.

diffraction patterns, collected as a function of scattering parameter (q) and of time (t), are presented. Bottom left 3D map shows a low-q perspective, while a high-q perspective 3D map is reported on the bottom right. Two map perspectives provide a better view of the entire process. As can be easily noticed, the intensity and width of some peaks undergo a modification, and the new reflections appear. In the upper plot, a comparison between the patterns collected after 10 min and after 160 h is presented. A 10 min pattern is characterized by a significant amorphous contribution, while in the last pattern, typical crystalline shape peaks are well-defined. Moreover, new reflections are now detectable, suggesting a new phase formation. The registered peaks show a good match with the hydroxyapatite phase: (200) at q = 1.44 (Å^{-1}), (002) at q = 1.83 (Å^{-1}), (210) at q = 2.00 (Å^{-1}), (211) at q = 2.24 (Å^{-1}), (130) at q = 2.76 (Å^{-1}), (203) at q = 3.13 (Å^{-1}) (calcium hydroxide phosphate, sys. hexagonal S.G. $P6_3/m$, card number 72-1243).[12]

To obtain more detailed information, two intense HA peaks, (210) and (211), were selected for the quantitative analysis, applying the Gaussian fit model. The obtained results are presented in Figure 2A,B. Figure 2A shows the time evolution of structural parameters, related to the (210) HA peak. The (210) HA Bragg reflection appears after 85 h of the process. After that, it undergoes a fast intensity increase (+350%). Grain dimensions do not change significantly, being about 17.0 ± 1.0 nm. Similar considerations can be made for the lattice parameter.

Figure 2B shows the time evolution of structural parameters, related to the (211) HA peak. The relative area kinetics is characterized by a typical sigmoid profile: during the first 83 h, it is constant and then a fast growth takes place until the final value is reached, after 96 h. Total increase is about +65% with a characteristic time of t = (87 ± 0.5) h. Similar considerations can be done regarding the curve reporting the grain size evolution, which is also characterized by a sigmoid profile. Initial grain dimensions are about 8 ± 1.0 nm. After about 82 h, a fast increase of the grain size was detected. The process is concluded after 88 h, reaching the final value of 11 ± 1.0 nm. The lattice parameter does not undergo significant changes during the whole duration of the process.

3.2. OCP + HL Cement. The diffraction patterns were collected every 10 min for the first hour and every 15 min for the following 69 h. Figure 3A shows a sequence of the EDXRD patterns collected upon the OCP + HL cement paste. An intense peak is visible in the central part of the diffraction pattern, attributable to the OCP phase ((260) Bragg reflection at q = 2.25 (Å^{-1})) (calcium hydrogen phosphate hydrate, sys. triclinic S.G. P1 (2), card number 26-1056).[12] As can be observed, no important changes were detected, apart from a small decrease of the overall diffracted intensity due to the evaporation of the liquid component. The conventional ADXRD experiments were performed to confirm this result (see Figure 3B). As can be noticed from Figure 3B, most of the OCP powder peaks are present in the final cement.

An accurate quantitative analysis of the (260) OCP Bragg reflection was performed for each pattern. A Gaussian fit model was used to extrapolate the structural information, the calculated average grain size being approximately 9.5 ± 1.0 nm.

SEM images collected after 1 h (A) and after 70 h (B) (Figure 4) of hardening confirm the obtained EDXRD and ADXRD results. No HA formation can be observed even at very high magnification (Figure 4B), the surface morphology being represented by the plate-shaped elongated OCP crystals.

3.3. OCP + HL + Chitosan Cement. The diffraction patterns were collected every 15 min for the total experimental time of 75 h. Figure 5 shows a 3D map of EDXRD patterns. The most intense (260) OCP Bragg reflection was registered at q = 2.25 (Å^{-1}). In the inset of Figure 5, a comparison between the first (0 h) and the last (75 h) pattern is shown. As can be observed, remarkable changes take place during the hardening process. New peaks, such as (210) at q = 2.00 (Å^{-1}), (211) at q = 2.24 (Å^{-1}), and (130) at q = 2.76 (Å^{-1}), attributable to the HA phase, appeared after approximately 3 ± 1 h, and some important changes occur during the entire hardening time. One of the most important is the intensity modulation of the two Bragg reflections (210) and (130). As shown in Figure 5, these reflections undergo a fast increase and decrease of the diffracted intensity, this modulation being clearly visible in Figure 6.

Gaussian model was applied for a quantitative analysis of the collected data. Gaussian fit was performed for two most representative peaks, (210) and (130). In Figure 6A, the time evolution of several structural parameters extrapolated by fitting the (210) HA Bragg reflection is shown: relative area, grain size, and lattice parameter. The (210) peak appeared 3 ± 1 h after the beginning of the experiment. An 110% increase of its relative area occurs during the first 7 h; afterward, a modulating behavior of the peak intensity takes place for the remaining 65 h. The modulations can be observed also for the grain size and

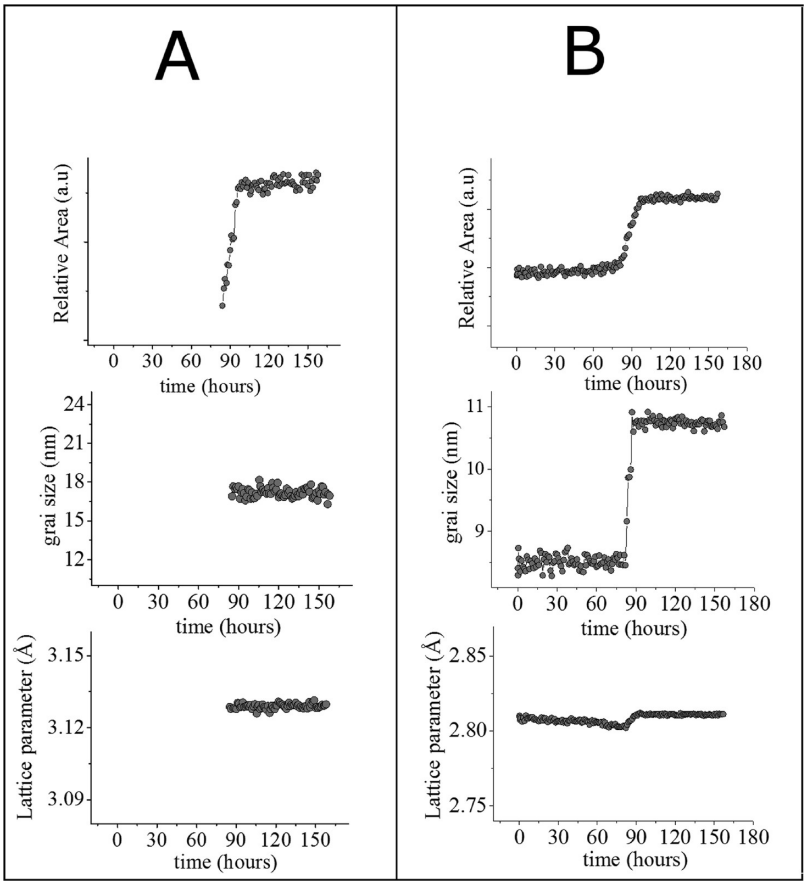

Figure 2. OCP soaked in SBF. (A) Time evolution of structural parameters related to (210) HA reflection: relative area, grain size, and lattice parameter. (B) Time evolution of the same structural parameters related to (211) HA reflection.

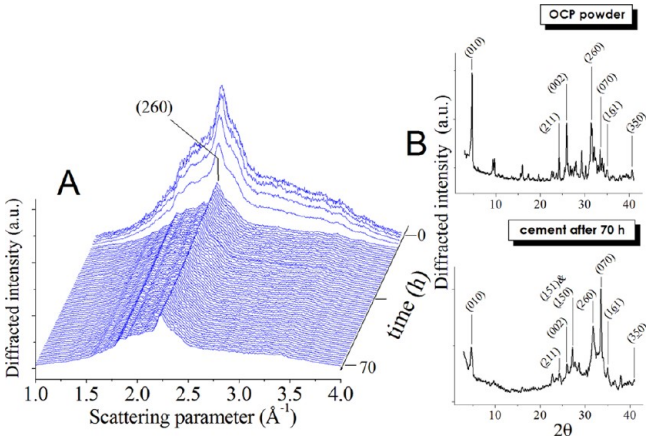

Figure 3. (A) Sequence of EDXRD patterns collected upon the OCP + HL cement. (B) Conventional ADXRD patterns of the OCP powder and of the OCP + HL cement after 70 h of hardening.

for the lattice parameter. Grain size periodically changes within the range of 12−18.5 (nm). The lattice parameter's time evolution is characterized by a modulation within the range of ±0.01 Å.

In Figure 6B, the time evolution of the same structural parameters extrapolated by fitting the (130) Bragg reflection is shown. The time evolution of the (130) Bragg reflection shows some similarities with the (210) reflection. Indeed, also this peak appears 3 ± 1 h after the beginning of the process. As visible from Figure 6B, it undergoes remarkable changes in its relative area and grain size. During the first 4 h, an increase of 300% and 100%, respectively, is registered. After such an increase, the same modulating behavior can be observed. In Figure 6B, a highlight of the (130) reflection time evolution, scattering parameter ranging from 2.6 to 3.2(Å^{-1}), is presented. In this highlight, this peculiar modulation of diffracted intensity is well distinguishable. The modulations continue for the whole duration of the experiment. Whereas, for the lattice parameter, only some slight changes were detected.

In Figure 7A−C, a selection of SEM images representing the evolution of the surface morphology of the OCP + HL + chitosan cement, as a function of the hardening time, is shown. As can be seen, the initial plate-shaped OCP crystals morphology (Figure 7A) gradually evolves into a much smoother, compact, and dense structure (B), likely due to the chitosan presence. Chitosan is known to have an aggregating and smoothing effect, conglomerating cement particles all together.[8] On the image collected after 75 h (Figure 7C), the presence of small HA crystals can be well noticed.

Authors[9] reported that OCP crystals are characterized by the plate-shaped elongated morphology and that small HA crystals appear likely as the result of de novo precipitation on the OCP crystal templates. Other literature data[16] also confirm that the thickening of OCP thin crystallites (in a certain crystallographic direction), thanks to their similarity to HA, provides a substrate for the HA nucleation and growth According to the SEM-EDXS analysis, the Ca/P ratio measured for small newly formed crystals was about 1.65−1.70, which indeed corresponds to the HA value.

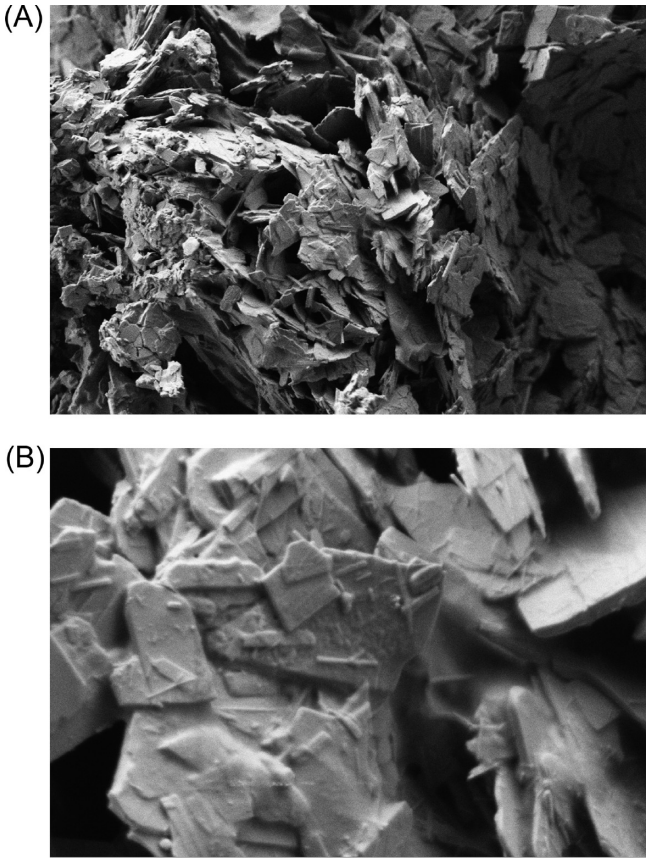

Figure 4. SEM images of the OCP + HL cement after: (A) 1 h (×15 000) and (B) 70 h (×75 000) of hardening.

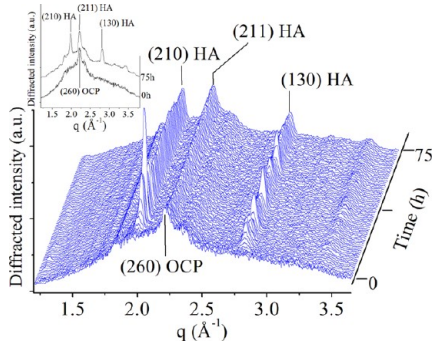

Figure 5. Sequence of EDXRD patterns collected upon the OCP + HL + chitosan cement. In the inset, a comparison between first (0 h) and last (75 h) collected pattern is shown.

3.4. OCP + HL + Chitosan Cement Soaked in SBF. In this experiment, the mild cement paste, after 15 min of its preparation, has been soaked in SBF. The spectra were collected for a total duration of 125 h. The diffraction patterns were collected every 10 min for the first hour and every 15 min for the following 124 h. In Figure 8, 3D map sequences of the EDXRD patterns are presented.

As can be noticed, a very peculiar hump-like shape time-profile characterizes this sequence of diffraction patterns. Another remarkable change is represented by the appearance of some new peaks. In the inset of Figure 8, the comparison between the patterns related to the beginning (0 h) and to the end (125 h) of the process is shown. As can be observed, some new reflections are present on the 125 h pattern (end of the process) with respect to the 0 h pattern. Consistently with the previous system (OCP + HL + chitosan), the new phase is attributable to HA: (002) at q = 1.83 (Å^{-1}), (210) at q = 2.00 (Å^{-1}), (211) at q = 2.24 (Å^{-1}), (130) at q = 2.76 (Å^{-1}), and (203) at q = 3.13 (Å^{-1}). All the new peaks appear approximately at t = (110 ± 1) h.

An accurate quantitative analysis of the (211) HA Bragg reflection was performed for each diffraction pattern. The obtained results are presented in Figure 9. The relative area follows a quasi-linear increase for the most part of the hardening process, then during the last 15 h an exponential growth take place, reaching a plateau for the last 4−5 h. Total increase of the peak relative area is about 300%. A fast exponential growth was detected for the lattice parameter, while the background intensity presents a peculiar "bump" shape, which is strictly related with the EDXRD pattern sequence profile shown in Figure 8. As to the grain size, an initial decrease takes place during the first 6−7 h; afterward, a modulating behavior characterizes its kinetic profile. Finally, an almost linear increase of the characteristic average dimension of the crystal domains was detected, until the final value of 9 nm has been reached.

In Figure 10, SEM micrographs, collected for morphological characterization of the evolving OCP + HL + chitosan + SBF cement system, are shown. In this case, despite the chitosan presence, no conglomerating effect was observed, likely due to addition of the SBF solution, which prevented densification of the cement mixture. The plate-shaped OCP crystals are present in all three images (Figure 10A−C). The appearance of small HA crystals can be noticed after 110 h of hardening (Figure 10B) and are very well seen (due to the phase contrast) at the end of the process (Figure 10C) (125h). This was confirmed by the SEM-EDXS analysis, since the Ca/P ratio measured for small newly formed crystals is about 1.65−1.70, corresponding to the HA value.

4. DISCUSSION

It is now recognized that the mineralization process of biological apatite involves the formation of metastable precursor phases. Therefore, it is important to study the final HA phase formation from such precursors. For biomaterials used for the bone tissue repair, the formation of hydroxyapatite, especially on their surface, is a desirable property, leading to the direct bonding between bone and material. In our case, the obtained experimental results evidence the HA formation in the following systems: OCP soaked in SBF, OCP + HL + chitosan cement, and OCP + HL + chitosan cement soaked in SBF, whereas, unexpectedly, no HA formation was detected during the OCP + HL cement hardening process.

When OCP is soaked in SBF, new HA phase appears after 85 h. Indeed, hydroxyapatite formation is not surprising in the systems with pH close to 7, like in our systems containing SBF. Authors[17] analyzed the driving force and nucleation rate of calcium phosphates precipitation in SBF, based on classical crystallization theories of thermodynamics and kinetics. The thermodynamic driving force for calcium phosphates precipitation was calculated on the basis of the classical equation of free energy change (ΔG) in supersaturated solutions. According to that study, the pH value is a critical factor that affects calcium phosphates precipitation. The HA precipitation is thermodynamically favorable ($\Delta G_{HA} < 0$) when pH ≥ 5.4. Under our experimental conditions (pH ≈ 7.4), $\Delta G_{HA} \approx -8$

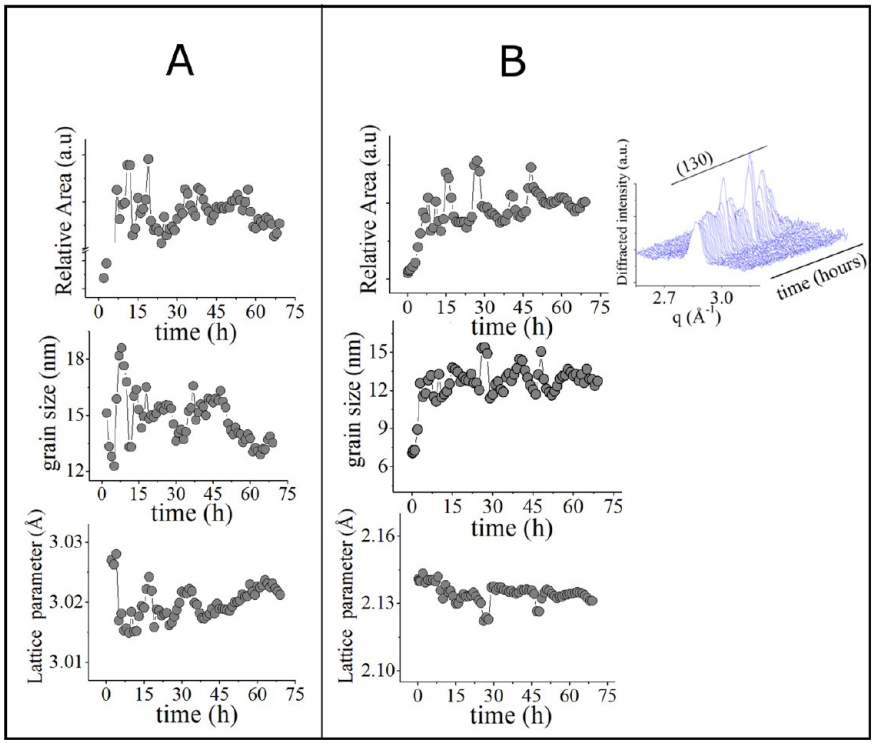

Figure 6. OCP + HL + chitosan cement. (A) Time evolution of structural parameters related to (210) HA Bragg reflection: relative area, grain size, and lattice parameter. (B) Time evolution of the same structural parameters related to (130) HA reflection.

and $\Delta G_{OCP} \approx -4$ and, therefore, the HA formation is more favorable.

In ref 18, the study of another system containing OCP is reported. Authors performed an EDXRD investigation of octacalcium phosphate transformation when mixed with physiological solution (aqueous isotonic 0.9% NaCl at pH ≈ 7.4). Also, in that case, the partial transformation of OCP into HA was registered.

In order to discuss why HA is not formed in the second investigated system (OCP + HL), it is essential to mention some general considerations for a calcium phosphate phase, such as OCP, in the presence of additives. It is clear that any discussion of the importance of OCP phase during the precipitation of calcium phosphates must take into account the influence of extraneous ions or molecules present in the solution.[19] In our case, the hardening liquid, which is sodium silicate solution, contains silicate and sodium ions. Extensive studies by LeGeros and co-workers, dedicated to the influence of different additives on the OCP transformation, were performed.[20−22] It was shown that the OCP hydrolysis is influenced by certain ions if present in solution: retarded by Mg^{2+}, citrate, and pyrophosphate, and accelerated by CO^{-}, HPO^{2-}, and Ca^{2+}. In our case, silicate or sodium ions might completely inhibit the HA formation. Therefore, the developed cement is composed of a single phase, such as OCP.

The presence of chitosan accelerates the OCP transformation into apatite, as it was shown for the OCP + HL + chitosan cement and for the OCP + HL + chitosan cement soaked in SBF. It should be noted that, for the OCP + HL + chitosan cement, the new HA phase appeared after 3 h. Whereas for the OCP + HL + chitosan cement soaked in SBF, it took 110 h; this latter result is likely due to the SBF solution presence.

Moreover, a modulating behavior of the peaks intensity and grain size was registered for the OCP + HL + chitosan cement and for the OCP + HL + chitosan cement soaked in SBF. Generally, it is believed that the OCP transformation into apatite occurs by dissolution and reprecipitation processes.[19] Once formed, HA remains as a stable phase, whereas OCP may further dissolve and hydrolyze, likely inducing such modulations. Therefore, the results obtained in this work could be considered as a support for the above-mentioned hypothesis. Analogous intensity modulation phenomenon was already registered and discussed in one of our previous studies dedicated to a bone cement based on anhydrous dicalcium phosphate.[23]

It should be noted that all the investigated OCP-based cement systems are composed of nanocrystals. According to the literature data,[24] nanocrystalline apatite cements are almost fully resorbed and replaced by the new bone 26 weeks after implantation. Likely, such fast osteotransduction is the result of the large specific surface area of nanocrystalline apatite, enhancing the osteoblast cell attachment.

5. CONCLUSIONS

The present study was focused on the in vitro behavior of the nanograin size cements (approximately in the range of 10−20 nm). Since the OCP-based bone cements are of great interest for biomedical applications, in this study, the EDXRD real-time monitoring of the hardening process of several OCP-based cements was performed. The SEM analysis confirmed and enriched the EDXRD results. The obtained experimental data evidence that, in the OCP soaked in SBF system, in the OCP + HL + chitosan cement, and in the OCP + HL + chitosan cement soaked in SBF, the new hydroxyapatite phase is formed, while, unexpectedly, no HA formation was registered during the OCP + HL cement hardening process. The tentative

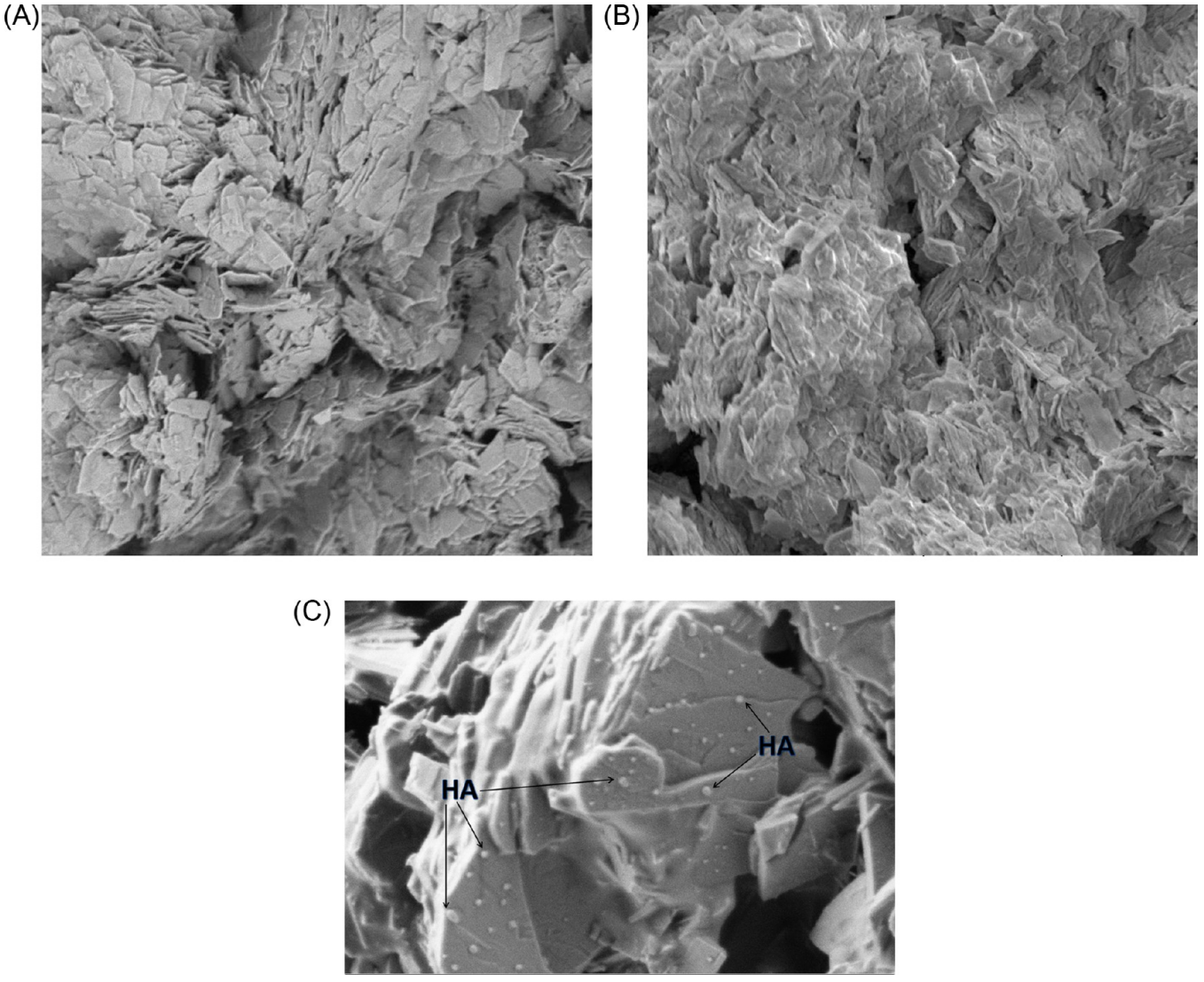

Figure 7. SEM images of the OCP + HL + chitosan cement after: (A) 1 h (×5000), (B) 2 h (×5000), and (C) 75 h (×75 000) of hardening.

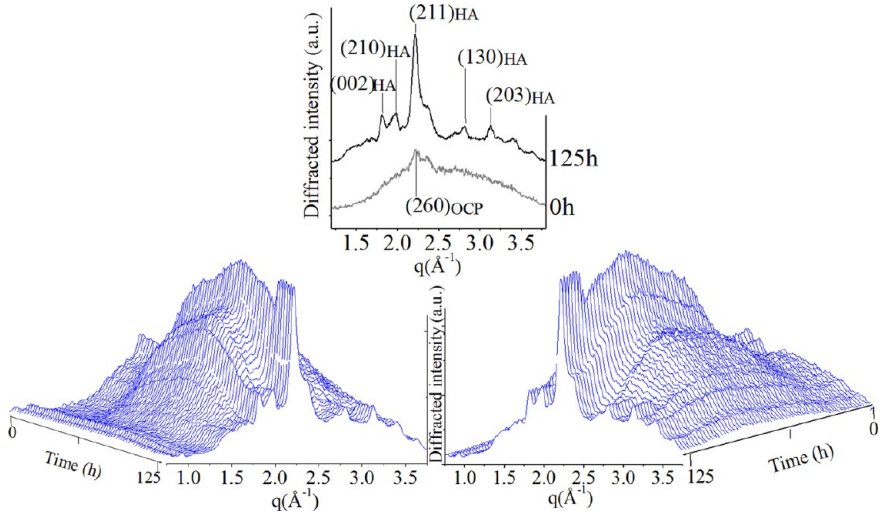

Figure 8. Sequence of EDXRD patterns collected upon the OCP + HL + chitosan + SBF cement. In the inset, a comparison between first (0 h) and last (125 h) pattern is shown.

explanation of the latter experimental fact is given by the probable influence of silicate and sodium ions, present in the hardening liquid and, possibly, inhibiting the HA formation. Therefore, according to the results of this work, the final HA

dx.doi.org/10.1021/am301809y | ACS Appl. Mater. Interfaces 2012, 4, 6202−6210

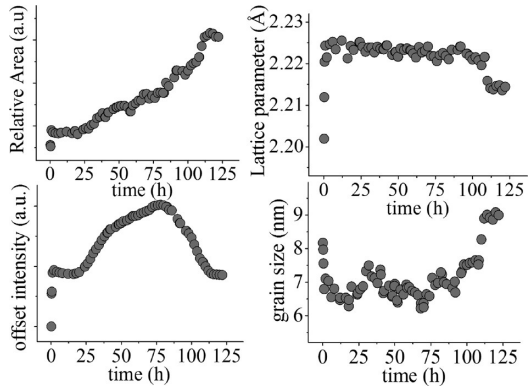

Figure 9. OCP + HL + chitosan + SBF cement. Time evolution of structural parameters related to (211) HA Bragg reflection: relative area, lattice parameter, offset intensity, and grain size.

phase is formed only in the presence of such additives as biopolymer chitosan and/or SBF, providing new insights into the biomineralization mechanism and new approaches for the present biomaterials technology.

AUTHOR INFORMATION

Corresponding Author

*Tel: +39-06-4993-4086. Fax: +39-06-4993-4153. E-mail: giulietta.rau@ism.cnr.it.

Notes

The authors declare no competing financial interest.

ACKNOWLEDGMENTS

Some of the authors are grateful to the Russian Foundation for Basic Research (RFBR), Grant No. 12-03-00079-a, for the partial financial support. A.Y.F. thanks "OPTEC" LLC providing a grant for "Young Russian Scientists".

REFERENCES

(1) Dorozhkin, S. V. *Materials* **2009**, *2*, 221−291.

(2) Barrere, F.; Van Blitterswijk, C. A.; De Groot, K. *Int. J. Nanomed.* **2006**, *1* (3), 317−332.

(3) Kuznetsov, A. V.; Fomin, A. S.; Veresov, A. G.; Putlyaev, V. I.; Fadeeva, I. V.; Barinov, S. M. *Russ. J. Inorg. Chem.* **2008**, *53* (1), 1−5.

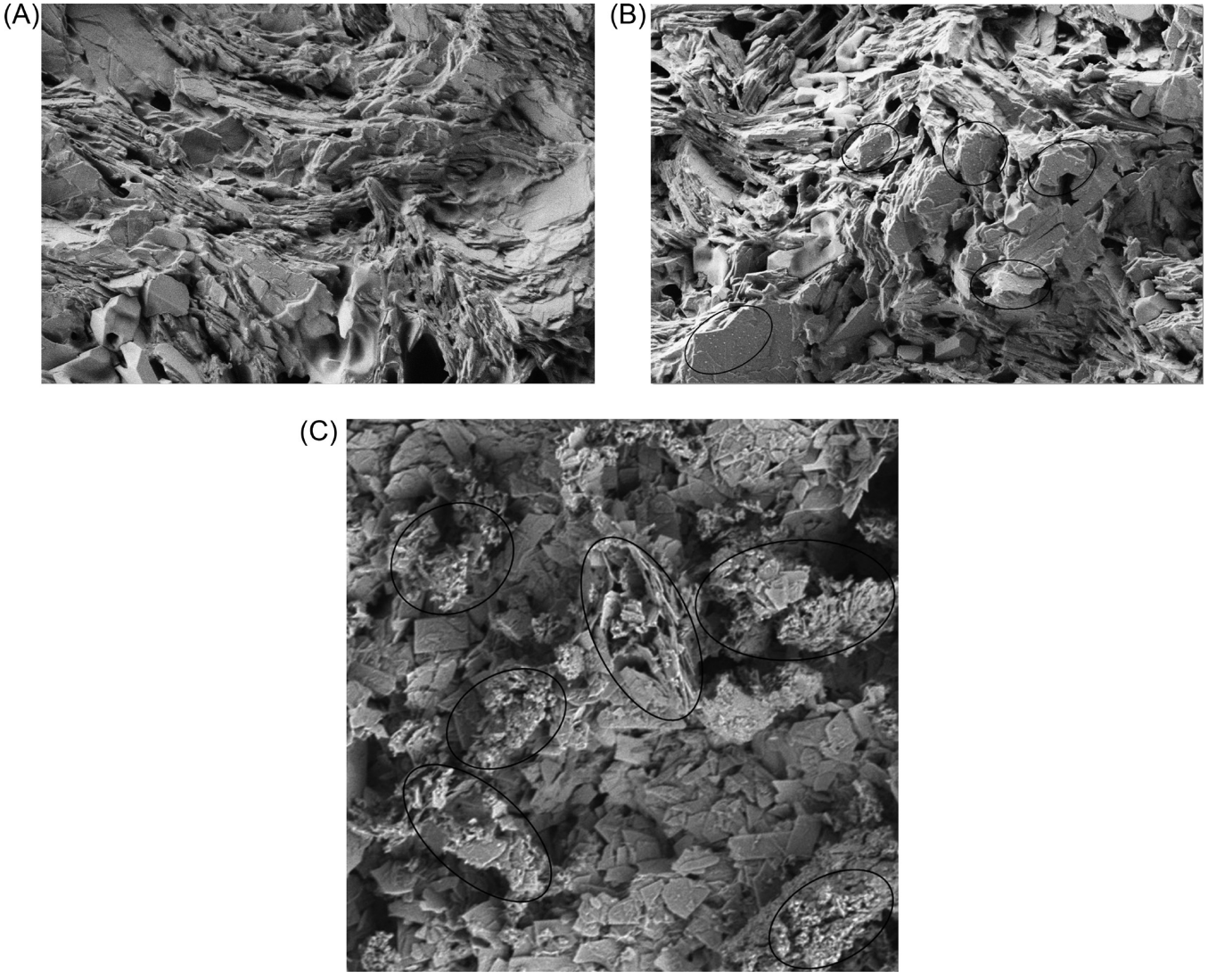

Figure 10. SEM images of the OCP + HL + chitosan + SBF cement after: (A) 1 h (×15 000), (B) 110 h (×15 000), and (C) 125 h (×5000) of hardening. In the (B) and (C) images, the areas of the appearance of small hydroxyapatite crystals are evidenced by the black circles.

(4) Barrere, F.; Van der Valk, C. M.; Dalmeijer, R. A. J.; Meijer, G.; Van Blitterswijk, C. A.; De Groot, K.; Layrolle, P. *J. Biomed. Mater. Res., Part A* **2003**, *66A* (4), 779−788.
(5) Shelton, R. M.; Liu, Y.; Cooper, P. R.; Gbureck, U.; German, M. J.; Barralet, J. E. *Biomaterials* **2006**, *27* (14), 2874−2881.
(6) Kamakura, S.; Sasano, Y.; Suzuki, O. *Interface Oral Health Sci.* **2005**, *1284*, 290−295.
(7) Rau, J. V.; Generosi, A.; Smirnov, V. V.; Ferro, D.; Rossi Albertini, V.; Barinov, S. M. *Acta Biomater.* **2008**, *4* (4), 1089−1094.
(8) Smirnov, V. V.; Rau, J. V.; Generosi, A.; Rossi Albertini, V.; Ferro, D.; Barinov, S. M. *J. Biomed. Mater. Res., Part B* **2010**, *93B*, 74−83.
(9) Rau, J. V.; Fosca, M.; Komlev, V. S.; Fadeeva, I. V.; Rossi Albertini, V.; Barinov, S. M. *Cryst. Growth Des.* **2010**, *10*, 3824−3834.
(10) Rau, J. V.; Generosi, A.; Komlev, V. S.; Fosca, M.; Fomin, A. S.; Barinov, S. M.; Rossi Albertini, V. *Dalton Trans.* **2010**, *39*, 11412−11423.
(11) Komlev, V. S.; Fadeeva, I. V.; Fomin, A. S.; Shvorneva, L. I.; Ferro, D.; Barinov, S. M. *Dokl. Chem.* **2010**, *432*, 178−182.
(12) *Database JCPDS*; International Centre for Diffraction Data: Newtown Square, PA, 2000.
(13) Orlov, Y. I. *Glass Phys. Chem.* **2001**, *28*, 281−287.
(14) Kokubo, T.; Kushitani, H.; Sakka, S.; Kitsugi, T.; Yamamuro, T. *J. Biomed. Mater. Res.* **1990**, *24*, 721−734.
(15) Generosi, A.; Smirnov, V. V.; Rau, J. V.; Rossi Albertini, V.; Ferro, D.; Barinov, S. M. *Mater. Res. Bull.* **2008**, *43*, 561−571.
(16) Meyer, J. L.; Eanes, E. D. *Calcif. Tissue Res.* **1978**, *25*, 209−216.
(17) Lu, X.; Leng, Y. *Biomaterials* **2005**, *26*, 1097−1108.
(18) Rau, J. V.; Komlev, V. S.; Generosi, A.; Fosca, M.; Rossi Albertini, V.; Barinov, S. M. *J. Cryst. Growth* **2010**, *312* (14), 2113−2116.
(19) Johnsson, M. S.; Nancollas, G. H. *Crit. Rev. Oral Biol. Med.* **1992**, *3*, 61−82.
(20) LeGeros, R. Z.; Kijkowska, R.; LeGeros, J. P. *Scanning Electron Microsc.* **1984**, *4*, 1771−1777.
(21) LeGeros, R. Z.; Kijkowska, R.; Abergas, T.; LeGeros, J. P. *J. Dent. Res.* **1986**, *65*, 293.
(22) LeGeros, R. Z.; Daculsi, G.; Orly, I.; Abergas, T.; Torres, W. *Scanning Electron Microsc.* **1989**, *3*, 129−137.
(23) Generosi, A.; Rau, J. V.; Komlev, V. S.; Rossi Albertini, V.; Fedotov, A.; Yu.; Barinov, S. M. *J. Phys. Chem. B* **2010**, *114* (2), 973−979.
(24) Van den Vreken, N. M. F.; Pieters, I. Y.; Declercq, H. A.; Cornelissen, M. J.; Verbeeck, R. M. H. *Acta Biomater.* **2010**, *6*, 617−625.